Industrial Crops & Products 240 (2026) 122630

Contents lists available at ScienceDirect

Industrial Crops & Products

journal homepage: www.elsevier.com/locate/indcrop

Low-temperature $ZnCl_2$ activation of distinct *Miscanthus* lignin as highly-porous biochar assembly for efficient removal of organic dyes, tetracycline and Cr(VI)

Junsheng Yu [a], Zongtai Tang [a], Lei Zhu [a], Bing Gao [a], Jing Hong [a], Yujia Fang [a], Jiacheng Kang [a], Dan Sun [b], Hao Peng [a], Boyang He [a], Mahmoud M.A. Bakr [c,d], Yanting Wang [a], Liangcai Peng [a,c], Hua Yu [a,*]

[a] Key Laboratory of Fermentation Engineering (Ministry of Education), Hubei Key Laboratory of Industrial Microbiology, National "111" Center for Cellular Regulation & Molecular Pharmaceutics, Biomass & Bioenergy Research Center, School of Life & Health Sciences, Hubei University of Technology, Wuhan 430068, China
[b] School of Material Science & Chemical Engineering, Hubei University of Technology, Wuhan 430068, China
[c] College of Plant Science & Technology, Huazhong Agricultural University, Wuhan 430070, China
[d] Agricultural & Biosystems Engineering Department, Faculty of Agriculture, Damietta University, Damietta 34517, Egypt

ARTICLE INFO

Keywords:
Miscanthus accession
Lignin-derived biochar
$ZnCl_2$ activation
Selective adsorption
Low-temperature pyrolysis
Adsorbent reusability

ABSTRACT

Efficient removal of diverse organic and inorganic pollutants from wastewater remains a critical challenge. Although lignocellulose-derived biochar is a green adsorbent, its selectivity and adsorptive capacity are still limited for large-scale application. As *Miscanthus* is a dedicated bioenergy crop providing abundant lignin-rich biomass, this study first extracted lignin fractions from two *Miscanthus sacchariflorus* accessions (Msa01 and Msa24) with distinct guaiacyl (G) and *p*-hydroxyphenyl (H) monomer proportions, and then generated biochar samples using $ZnCl_2$ as an activating agent at various temperatures. Among the total of 20 biochar samples obtained, two optimal biochar samples were obtained at 400°C, a significantly lower temperature relative to the most chemical-activations processes, but they both exhibited exceptionally high specific surface areas (>1500 m^2/g) with distinct pore architectures, leading to size- and type-selective adsorptions. By comparison, the Msa01 biochar possessed a relatively smaller average pore size and volume than those of the Msa24 biochar, enabling superior uptake of the small dye methylene blue (541.9 mg/g), whereas the Msa24 biochar sample preferentially adsorbed larger organic molecules such as Reactive Blue 19 (1286.1 mg/g) and Tetracycline (731.9 mg/g). Both biochar samples also achieved effective removal of the inorganic contaminant Cr(VI) (381.2–392.1 mg/g), attributed to their exceptionally high surface areas and pore volumes. Adsorption isotherm and kinetic analyses indicated multilayer adsorption on the heterogeneous surfaces governed by active site availability, and molecular dynamics simulations further revealed that adsorption was driven by strong non-covalent interactions. In addition, two biochar samples showed excellent recyclability, retaining up to 97 % of initial adsorption capacity after five cycles. This work thus demonstrates a sustainable and energy-efficient strategy for valorizing lignin-rich agricultural residues into hierarchical porous biochar with tunable molecular-size selectivity for remediation of multiple pollutants.

1. Introduction

Miscanthus is a high-yielding perennial grass widely recognized as a promising biomass feedstock due to its short growth cycle, high biomass productivity, and strong adaptability to marginal lands (Cheng et al., 2018; Wang et al., 2016). As a typical energy crop, *Miscanthus* straw has demonstrated a broad application potential in thermochemical conversion, environmental remediation, functional material production, and carbon material fabrication (Sun et al., 2017). Its lignocellulose is rich in cellulose and lignin, which are responsible for its favorable properties in thermochemical conversion into high-quality carbon materials (Wang et al., 2024a). Unlike the hemicellulose, which decomposes at relatively low temperatures, the abundant lignin component possesses a high degree of aromaticity and thermal

* Correspondence author.
E-mail address: yuhua@hbut.edu.cn (H. Yu).

https://doi.org/10.1016/j.indcrop.2026.122630
Received 30 October 2025; Received in revised form 26 December 2025; Accepted 2 January 2026
Available online 10 January 2026

resistance. Consequently, efficient utilization of *Miscanthus* lignocellulose not only contributes to the valorization of agricultural waste into industrial bioproducts, but also offers a sustainable and green material for environmental remediation (An et al., 2025).

Lignin is an aromatic polymer composed of *p*-hydroxyphenyl (H), guaiacyl (G), and syringyl (S) units linked by ether (e.g., β–O–4, α–O–4) and C–C bonds (Ai et al., 2024; Fu et al., 2022; Yu et al., 2025). The composition and degree of cross-linking among these structural units directly influence the thermal stability and carbonization behavior of lignin (Li et al., 2020). Compared to cellulose and hemicellulose, lignin possesses a higher degree of aromaticity and carbon content, which facilitates the formation of stable carbon skeletons and higher char yields during pyrolysis (Li et al., 2024b; Wang et al., 2018). Therefore, lignin-rich biomass is particularly suitable for the production of high-performance biochar with large specific surface areas, stable structures, and abundant aromatic functionalities, which are the critical factors for effective adsorption and immobilization of organic pollutants (Egun et al., 2025).

Biochar, a carbonaceous material generated by pyrolyzing biomass under oxygen-limited conditions, is characterized by high porosity, abundant surface functional groups, excellent thermal stability, and high tunability (Hu et al., 2023; Liu et al., 2023; Zhang et al., 2023b). In recent years, it has attracted considerable attention in water pollution remediation (Laishram et al., 2025). For improving biochar adsorption performance, chemical activation is widely employed as an effective modification strategy (Zhou et al., 2024). Among various activating agents, $ZnCl_2$, a Lewis acid-type chemical, stands out for its ability to promote biomass dehydration, condensation, and aromatization (Ali et al., 2025). Although $ZnCl_2$ activation is more compatible and effective in the thermal-chemical conversions of lignocellulose feedstocks rich in lignin compared to alkaline (e.g., KOH, NaOH) and acidic (e.g., H_3PO_4) activation methods (Memetova et al., 2022; Serra-Parareda et al., 2020), the specific influence of the intrinsic lignin monomer ratio on the pore evolution mechanism during $ZnCl_2$ activation remains poorly understood.

The growing release of hazardous pollutants such as major industrial dyes (e.g., methylene blue/MB; reactive blue/RB), antibiotics (tetracycline/TC), and heavy metals (Cd, Pb, Cr) has posed severe challenges to environmental remediation (Wang et al., 2025c). These contaminants are persistently toxic, poorly biodegradable or non-degradable, and are commonly discharged in effluents from textile, pharmaceutical, agricultural, and electroplating industries, posing significant threats to ecosystems and human health (Patel et al., 2024). Compared to traditional water treatments, the biochar-based adsorption offers advantages such as high efficiency, cost-effectiveness, operational simplicity, and renewability, presenting a promising approach for organic and inorganic contaminant removal (Singh and Maiti, 2024).

In this study, two types of lignin-rich *Miscanthus* feedstocks (Msa01 and Msa24) were employed to produce porous biochar via a $ZnCl_2$-assisted activation strategy at exceptionally low temperatures. The role of $ZnCl_2$ activation in modulating the biochar structure was elucidated, and the adsorption performance of the resulting biochar toward typical organic dyes (MB and RB), tetracycline (TC) and heavy metal (Cr(VI)) was systematically evaluated by assessing the impact of biomass source on the structural characteristics and adsorption behavior. This work thus provides new insights into lignin-based carbon materials and offers a feasible strategy for the high-value utilization of agricultural residues and the effective removal of industrial organic and inorganic pollutants.

2. Materials and methods

2.1. Collection of biomass samples

The general procedure of major experiments performed in this study was illustrated in Fig. S1. Two *Miscanthus* (Msa01 and Msa24) accessions were selected from a germplasm resource and cultivated under uniform agronomic conditions in the Experimental Field of Huazhong Agricultural University (Wuhan, China) (Li et al., 2016). The well-dried biomass was milled using a QE-300 grinder, passed through a 40-mesh sieve, and the resulting powder was stored until use.

2.2. Wall polymers extraction and determination

Plant cell wall fractionation was performed as described previously (Liu et al., 2021a). An ultraviolet-visible (UV–VIS) spectrometer (V-1100D; Shanghai MAPADA Instruments Co.) was used for hexose, pentose, and uronic acid assays, as previously described (Wang et al., 2024b, 2025d). The total lignin content was determined using a two-step acid hydrolysis method according to the Laboratory Analytical Procedure of the National Renewable Energy Laboratory. All assays were performance in independent triplicates (Yu et al., 2022).

2.3. Lignin extraction

Two lignin-extraction methods were employed in this study by using alkaline and acid solutions, respectively. For alkaline extraction, straw powder was mixed with a 15 % (w/w) sodium hydroxide solution at a solid-to-liquid ratio of 1:15 and heated at 90 °C under continuous stirring for 4 h. After extraction, the resulting supernatant was adjusted to pH 2 using 20 % sulfuric acid to precipitate the lignin. The precipitate was then washed with deionized water until neutral and dried to a constant weight (Zhang et al., 2023a). For acid extraction, straw powder was initially mixed with 67 % sulfuric acid at a solid-to-liquid ratio of 1:10 and shaken at room temperature for 1.5 h. The mixture was washed to neutrality, and the solid residue was subjected to a second hydrolysis step using 2.88 % sulfuric acid at 120 °C for 1 h at a solid-to-liquid ratio of 1:20. The final residue was thoroughly washed to remove residual acid and dried to a constant weight as previously described (He et al., 2022).

2.4. Determination of lignin monomer content

Monolignols were extracted by Nitrobenzene Oxidation as described (Li et al., 2014). Standard H-, G- and S-monolignols were purchased from Sinopharm Chemical Reagent Co., Ltd. A Kro-mat Universal C18 column (4.6 mm × 250 mm, 5 μm) was used for HPLC analysis using a SHIMADZU LC-20A machine with a UV-detector at 280 nm. CH_3OH: H_2O:HAc (16:63:1, v/v/v) was used as mobile phase (flow rate: 1.1 mL/min), and the injection volume was 20 μ as described previously (Zhang et al., 2021b).

2.5. Biochar preparation

Lignin and $ZnCl_2$ were first mixed at a mass ratio of 1:2 and subjected to carbonization at temperatures ranging from 300 °C to 800 °C (with 100 °C increments) to identify the optimal pyrolysis temperature for biochar preparation at 400 ℃. Subsequently, a series of activation ratios (lignin: $ZnCl_2$ = 1:1, 1:2, 1:3, 1:4, 1:5, w/w) were conducted at the selected temperature (400 °C) to optimize the activation conditions. All carbonization experiments were conducted in a tube furnace (OTF-1200X, Hefei Kejing Materials Technology CO., LTD) under a nitrogen flow. The samples were heated at a rate of 5 °C/min to the designated temperature and maintained for 2 h to ensure complete carbonization. Afterwards, the furnace was cooled to 300 °C at a rate of 10 °C/min and then allowed to cool naturally to room temperature. The obtained biochar was collected and dispersed in 200 mL of distilled water, stirred for 6 h, and washed repeatedly with distilled water until the filtrate reached pH 7.0. Finally, the washed biochar was dried at 60 °C to constant weight and stored until use (Li et al., 2024c).

2.6. Analysis of organic and inorganic pollution adsorption with biochar

Methylene Blue (MB, CAS: 61–73–4), Reactive Blue 19 (RB, CAS: 2580–78–1), tetracycline (TC, CAS: 64–75–5) solutions were prepared in ultrapure water at room temperature (25 ± 1 °C). For each adsorption test, 20 mL of solution was mixed with 20 mg of biochar in a conical flask and shaken at 150 rpm for 6 h in a thermostatic shaker. The suspensions were filtered through 0.45 μm membrane filters to remove biochar particles. Residual dye concentrations were determined using a UV–Vis spectrophotometer (V1100D, Shanghai MAPADA Instrument Co., Ltd.) at 664 nm (MB), 595 nm (RB), and 360 nm (TC). All assays were completed at independent triplicates. For Cr(VI) adsorption, a stock solution (0.1 g/L) was prepared by dissolving 0.2829 g $K_2Cr_2O_7$ (CAS: 7778–50–9) (dried at 120 °C for 2 h) in 1000 mL distilled water. Working standards (1.0 and 5.0 μg/mL) were freshly prepared by dilution. The color reagent was prepared by dissolving 0.2 g diphenylcarbazide in 50 mL acetone and diluting to 100 mL with distilled water, and stored in the dark. For calibration, 50 mL of standard solution was mixed with 0.5 mL H_2SO_4 (1:1, v/v), 0.5 mL H_3PO_4 (1:1, v/v), and 2.0 mL color reagent. After 10 min, absorbance was recorded at 540 nm using distilled water as the blank. All assays were performance in independent triplicates (Wang et al., 2025c). The adsorption capacity of the biochar (q_e, mg/g) was calculated using the following equation:

$$q_e = \frac{(C_0 - C_e) \times V}{M} \tag{1}$$

Where C_0 (mg/L) and C_e (mg/L) indicate the concentration of MB or RB at initial and equilibrium. The volume of the solution is expressed as V (L) and the mass of the sample is expressed as M (mg) (Lima et al., 2019, 2021; Liu and Liu, 2008).The correlation between adsorption capacity (q_e, mg/g) and the concentration of MB, RB (C_e, mg/L) at equilibrium was modeled using three isotherms. The Langmuir isothermal equation is given below:

$$q_e = q_{th}^e \frac{K_{eq} C_e}{1 + K_{eq} C_e} \tag{2}$$

Among them, q_{max} refers to the maximum adsorption capacity (mg/g), Keq represents the Langmuir isothermal constant, refereeing the adsorption capacity of biochar for MB or RB (Liu and Liu, 2008). The Freundlich isotherm equation is stated as follow:

$$q_e = K_F C_e^{1/nF} \tag{3}$$

Where, K_F is the Freundlich isotherm constant, and $1/n$ is the heterogeneity factor (Lima et al., 2019).

The equation of Temkin model is given as follow:

$$q_e = \frac{RT}{b} Ln(K_T C_e) \tag{4}$$

Where, K_T (L/mol) refers to the equilibrium constant, b (J/mol) is the Temkin constant related to adsorption heat, R is the universal gas constant, and T is the absolute temperature (K) (Fan et al., 2024a). The kinetics models were applied to predict the relationship between adsorption capacity at equilibrium (q_e, mg/g) and adsorption for t hours (q_t, mg/g). The pseudo 1st order model (Eq. 5) and pseudo 2nd order model (Eq. 6) are presented as follows:

$$\frac{\partial q_t}{\partial t} = k_1^{'}(q_e - q_t) \tag{5}$$

$$\frac{dq_t}{dt} = k'_2(q_e - q_t)^2 \tag{6}$$

Where k_1 and k_2 are the pseudo 1st order and pseudo 2nd order constants, respectively (Lima et al., 2021). The Weber–Morris intraparticle diffusion model is stated as:

$$q_t = k_{ip} t^{0.5} + C \tag{7}$$

Where, k_{ip} is intraparticle diffusion apparent adsorption rate constant, C is a constant related to the boundary layer thickness (Lima et al., 2019).

2.7. Adsorbent recycling detection

The biochar reusability was assessed through successive adsorption–desorption cycles. After each adsorption experiment, the spent biochar was washed with 40 mL of 95 % ethanol and shaken at 150 rpm and 25 °C for 1 h to desorb organic dye. The ethanol solution was replaced every hour until the dye was completely desorbed, as determined by the absence of color in the ethanol wash. The adsorption–desorption cycle was repeated five times. All experiments were performed in triplicate to ensure statistical reliability (Mutabazi et al., 2024).

2.8. Reutilization of the activating agent

To recover the $ZnCl_2$ activating agent, 100 mL of 10 % hydrochloric acid (HCl) solution was added to the used biochar in a 250 mL Erlenmeyer flask. The mixture was shaken at room temperature for 1 h and then filtered to collect the supernatant containing Zn^{2+} ions. Subsequently, 2 g lignin was added to the filtrate, and the mixture was magnetically stirred for 6 h. The resulting suspension was oven-dried at 60 °C to obtain lignin impregnated with reused $ZnCl_2$, which was then used for the next round of biochar preparation. All experiments were performed in triplicate (De Smedt et al., 2025).

2.9. Characterization of lignin and biochar samples

The physicochemical properties of lignin and biochar samples were systematically assessed using various analytical techniques. Specific surface area and pore structure were determined by nitrogen adsorption–desorption isotherms using the Brunauer–Emmett–Teller (BET) method (ASAP 2460, Micromeritics, USA). Surface elemental composition and chemical states were analyzed by X-ray photoelectron spectroscopy (XPS, Thermo Scientific ESCALAB Xi+). Surface morphology was observed via scanning electron microscopy (SEM, ZEISS, Germany). Structural features were characterized by Raman spectroscopy (ATR8300 Series), while crystalline phases were identified using X-ray diffraction (XRD, FRINGE CLASS). Thermal stability was examined through thermogravimetric analysis (TGA, NETZSCH STA 2500). Elemental composition was determined using an elemental analyzer (EMA502), and functional groups were identified by Fourier-transform infrared spectroscopy (FTIR, Nicolet iS10, Thermo Fisher Scientific, USA).

2.10. Two-dimensional correlation spectroscopy (2D-COS) analysis

The correlated infrared spectra of 2D-PCIS are divided into synchronous $\Phi(\nu_1, \nu_2)$ and asynchronous $\psi(\nu_1, \nu_2)$, in which ν_1 and ν_2 represent the consistency of the intensity of the two Raman peaks when subjected to external perturbations, respectively. The asynchronous 2D correlation intensities were used to account for the difference in the order or rate of change in the intensity of the two Raman peaks (ν_1 and ν_2) while subjected to external perturbations. By combining synchronous and asynchronous spectral analysis, the relative change priority of ν_1 and ν_2 was determined, and the detailed determination method is based on the Noda rule (Yang et al., 2024).

2.11. Molecular dynamic simulation

The biochar model was constructed in Gaussian09/GaussView software based on the elemental composition obtained from an elemental

analyzer. The chemical structures of RB and MB dye molecules were downloaded and modified from the chemical structure database PubChem (https://pubchem.ncbi.nlm.nih.gov/). Molecular dynamics simulations were performed by the GROMACS package (2019.6 version) (Abraham et al., 2015). Leap-frog algorithm was used to solve Newton's equations of motion with a time step of 2 fs. Hydrogen-involved covalent bonds were constrained throughout the ensemble and production runs with the LINCS algorithm, which allowed motion with a time step of 2 fs for the leap-frog algorithm to solve the Newton's equations (Hess et al., 1997). A grid-based neighbor searching algorithm was used with a 0.8 nm cutoff for both short-range Coulombic and van der Waals interactions. Long-range electrostatics were treated by the Particle Mesh Ewald (PME) method. A velocity-rescale thermostat was used to regulate the temperature at 300 K with a time constant of 0.5 ps (Bussi et al., 2007), and isotropic pressure coupling was controlled at 1.0 bar using Berendsen barostat, with a time constant of 1.0 ps and compressibility of 4.5×10^{-5} bar^{-1} (Berendsen et al., 1984). Periodic boundary conditions were applied in all three dimensions. Box sizes were set as a box of $2 \times 2.3 \times 6.2$ nm^3. SPC216 water model was used to solvate the simulation boxes (Mark and Nilsson, 2001). Steepest descent minimization algorithm were used to the system. The system was first subjected to NVT equilibration for 5 nanoseconds (ns), followed by 5 ns of NPT equilibration, and then a 20 ns molecular dynamics simulation was performed in an aqueous environment, and the 20 ns was used for statistical analysis using GROMACS tools. Molecular images in this work were rendered by VMD 1.9.3 (Humphrey et al., 1996).

2.12. Statistical analysis

The line graph, histogram, and for the best-fit curve were plotted using the Origin software (OriginLab, USA). Student's *t*-test and analysis of variance (ANOVA) were performed using the SPSS 23 software (IBM, USA).

3. Results and discussions

3.1. High-performance biochar via $ZnCl_2$ activation at low temperature

Two representative *Miscanthus* accessions (Msa01 and Msa24) were selected from the previously established *Miscanthus* germplasm resources (Fig. S2). Based on chemical analyses, two *Miscanthus* accessions showed similar cell wall compositions including similar levels of four major polymers (cellulose, lignin, hemicellulose, pectin) (Fig. S2, Fig. 1A), but different G- and H-monomers proportions were detected between the two accessions (Fig. 1B). In particular, the Msa01 lignin contained 35.4 % more G-monomer and 20.5 % less H-monomer compared to the Msa24 one, indicating that two *Miscanthus* accessions could provide the desirable lignin substrates distinctive in their G- and H-monomers proportions. With respect to two *Miscanthus* accessions containing distinct lignin compositions, this study employed classic acid hydrolysis (H^+, Klason method) and alkaline extraction (OH^-, NaOH) to extract lignin substrates, respectively. And then performed $ZnCl_2$-activated thermochemical conversions for biochar production at three temperatures (400 °C, 600 °C, 800 °C) (Fig. 1C). As a comparison, the three biochar samples generated from alkali-extracted lignin substrate showed consistently higher MB adsorption capacities than those of the acid-extracted counterparts, with an average increase in adsorption capacity ranging from 32.1 % to 74.3 % (Fig. 1D & E), suggesting that OH^- lignin may contain more functional groups favorable for interactions with $ZnCl_2$ during activation. Notably, the $ZnCl_2$-activated biochar prepared at 400 °C exhibited the highest MB adsorption capacity among the previously-reported biochar samples, including highly adsorptive materials generated using other chemical activations at higher temperatures (Ahmed et al., 2019; Chen et al., 2019; De

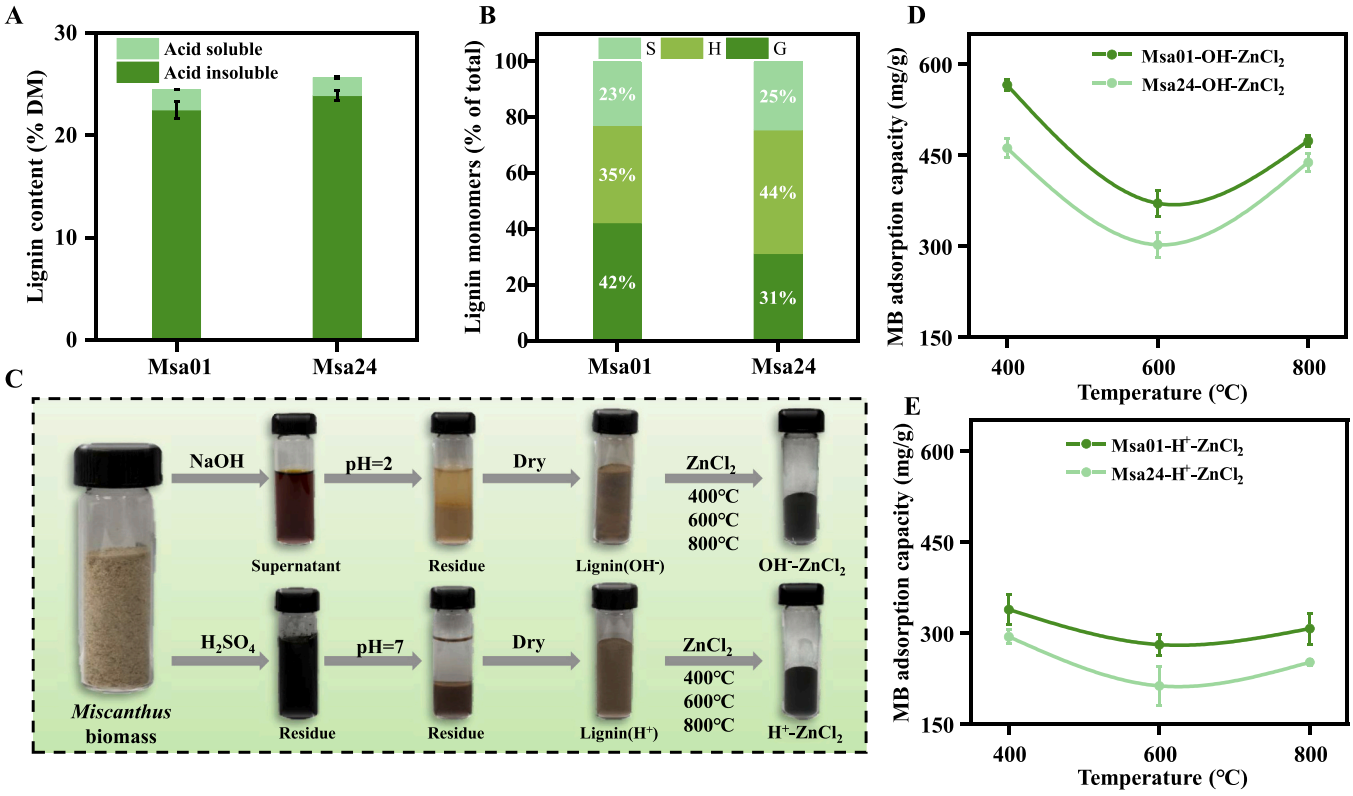

Fig. 1. Lignin extraction and biochar preparation for methylene blue (MB) adsorption using mature straws of two *Miscanthus* accessions (Msa01, Msa24). (A) Total lignin content; (B) Monolignol composition; (C) Schematic illustration of lignin extraction for biochar generation; (D) (E)Adsorption capacity of $ZnCl_2$-activated biochar prepared at three temperatures; Data as means ± SD (n = 3) with Student's *t*-test as significant differences between Msa01 and Msa24 samples at $^{**}p < 0.01$ or $^{*}p < 0.05$. Adsorption conditions: T (temperature) = 25 °C, dosage = 1.0 g/L, t (time) = 6 h.

Benedetto et al., 2020; Du et al., 2017; Fan et al., 2025; Jahani et al., 2023; Liu et al., 2021b; Lv et al., 2020; Mbarki et al., 2022; Sun et al., 2022; Wang et al., 2025a, 2025c; Zhang et al., 2022). To further validate previous reports, this study also prepared the KOH-activated biochar under three temperatures, and two biochar samples generated at 400 °C had the lowest MB adsorption capacities among all six biochar samples (Fig. S3), which were by 5.4-fold (Msa01) and 16.7-fold (Msa24) lower relative to the MB adsorption capacities of the $ZnCl_2$-activated biochar samples at 400 °C. In addition, all biochar samples prepared from Msa01 accession maintained consistently higher MB adsorption capacities than those of Msa24, which should be mainly due to the distinct G- and H-monomers proportions of lignin substrates between two *Miscanthus* accessions. Taken together, the combination of NaOH extraction and $ZnCl_2$ activation at 400 °C emerged as the most effective approach, offering a low-energy and high-efficiency route to fabricate high-performance adsorbents. It also suggests that the adsorption performance of lignin-derived biochar should be determined by a synergistic interplay among biomass type, lignin extraction method, and activation chemical.

3.2. Dynamic $ZnCl_2$ activations for diverse biochar assembly and performances

To understand the high-performance biochar production via $ZnCl_2$ activation at low temperature, a total of 20 biochar samples were prepared by performing pyrolysis of alkali-extracted lignin at six temperatures (300 °C-800 °C) and $ZnCl_2$ activation at six dosages (Fig. 2A & B). As a result, the optimal biochar samples of two *Miscanthus* accessions were identified by $ZnCl_2$ activation with lignin substrates ($ZnCl_2$: lignin at 2: 1) at 400 °C, and they exhibited the MB adsorptive capacities at 565.5 mg/g and 461.3 mg/g, respectively. XRD profiling revealed that $ZnCl_2$ was gradually converted into ZnO during pyrolysis, and the intensities of ZnO characteristic peaks were increased with rising pyrolysis temperatures (Fig. 2C & D). While a moderate amount of ZnO facilitates the pore formation in biochar, excessive ZnO may block pore channels to reduce the surface area and porosity, thus impairing adsorption performance (Xiang et al., 2025). Raman spectroscopic profiling showed a decreasing I_D/I_G ratio with increasing pyrolysis temperature, suggesting progressive graphitization and increased structural ordering (Fig. S4). Two-dimensional correlation Raman spectroscopy (2D-COS) further probed the thermally induced structural transitions of the biochar samples (Fig. 2E-H; Fig. S5). For the Msa01 biochar sample, the synchronous and asynchronous cross-peaks (1350 cm^{-1}, 1580 cm^{-1}) were positive for a sequential and cooperative transformation, resulting in disordered structures (D-band) responding earlier than the graphitic domains (G-band). In contrast, the Msa24 biochar sample exhibited a positive synchronous, but negative or negligible asynchronous cross-peak for a simultaneous and more homogeneous response of D- and G- bands to external perturbation, which accounted for a more ordered and stable carbon framework formed at higher pyrolysis temperatures. In addition, polar oxygen-containing functional groups (e.g., -OH, -COOH, -C═O) were retained to a greater extent at lower pyrolysis temperatures, which likely enhanced adsorption through hydrogen bonding, electrostatic interactions or complexation with dye molecules (Saha et al., 2019). As the pyrolysis temperatures were increasing, those functional groups were progressively removed due to carbon structure condensation and graphitization, resulting in a more hydrophobic surface and fewer active sites accountable for reduced adsorption capacity (Han et al., 2022). As the lignin-to-$ZnCl_2$ ratio increased from 1:1–1:5, the adsorption capacity first increased and then declined (Fig. 2B). Raman spectroscopy (Fig. S5) showed that the I_D/I_G ratio followed a similar trend, rising initially and then decreasing, suggesting that moderate $ZnCl_2$ addition could promote the development of disordered carbon structures and subsequently reorganize at higher loading. As 2D-COS analysis provides a deep insight into structural evolution (Fig. S5), the asynchronous spectral changes (with the G band responding earlier) thus revealed that the graphitic domains were progressively disrupted and converted into defect-rich structures during activation. These induced defects and disordered regions could act as primary "attack sites" for $ZnCl_2$ etching, and the defect-driven activation should directly facilitate the intensive development of pores, thereby creating exceptionally high specific surface area (Bergna et al., 2022). In detail, the G-rich precursor (Msa01) possessed free C5 positions on the aromatic ring, which facilitated the formation of condensed C-C linkages during carbonization for a rigid carbon framework abundant in structural defects. Meanwhile, $ZnCl_2$ preferentially attacked these defect regions, creating extensive porosity and resulting in the superior specific surface area as observed in the Msa01 sample. By contrast, the S-rich

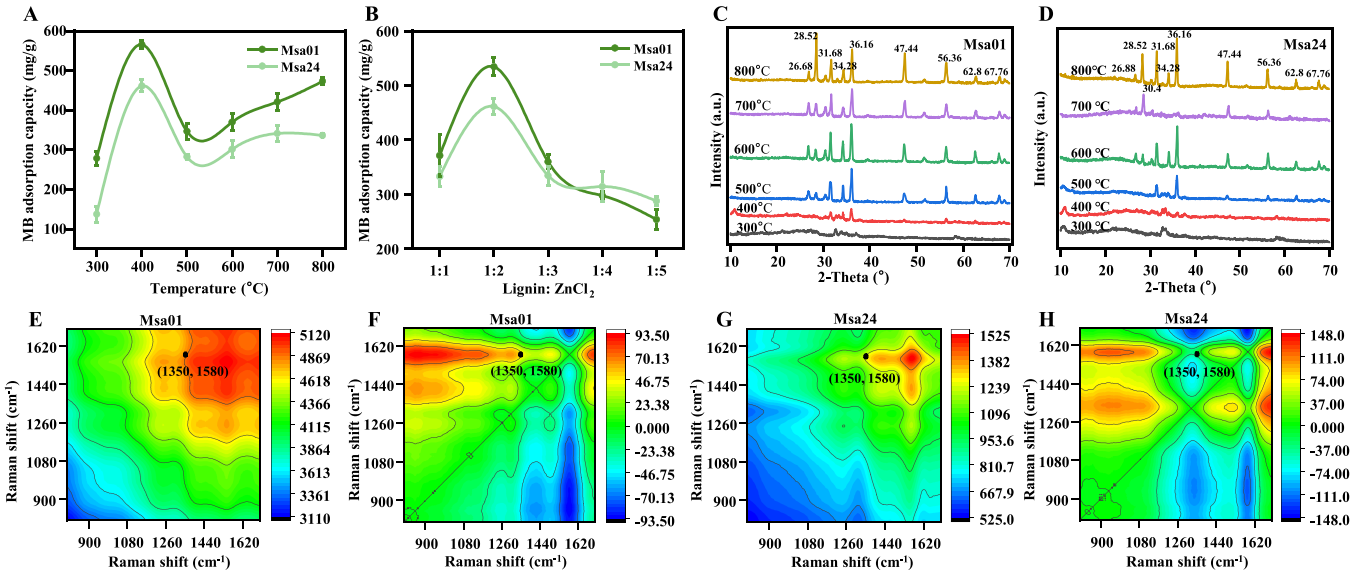

Fig. 2. Optimizing $ZnCl_2$ activation for biochar preparations using lignin substrates extracted from mature straws of two *Miscanthus* accessions (Msa01, Msa24). (A) MB adsorption capacity of the biochar samples prepared at different temperatures; (B) MB adsorption capacity of the biochar prepared with different proportions of $ZnCl_2$ at 400 °C; (C, D) XRD patterns of two biochar samples prepared at different temperatures; (E, G) Synchronous Raman spectra of Msa01 and Msa24 biochar samples as prepared at (C, D), respectively; (F, H) Asynchronous Raman spectra of Msa01 and Msa24 biochar samples. Adsorption conditions: T = 25 °C, dosage = 1.0 g/L, t = 6 h.

precursor (Msa24) contained methoxy groups that sterically hinder C-C cross-linking, which resulted in a more ordered and stable graphitic arrangement to make the carbon matrix more resistant to chemical etching, thereby limiting the development of porosity compared to the G-rich counterpart. Therefore, the distinct spectral behaviors of Msa01 and Msa24 samples can be attributed to their intrinsic molecular differences. XRD profiling confirmed that the proportion of $ZnCl_2$ significantly affected the crystalline structure and phase composition of the resulting biochar samples (Fig. S6). Hence, an appropriate amount of $ZnCl_2$ facilitates pore formation and increases specific surface area, thereby enhancing adsorption performance. In contrast, excessive $ZnCl_2$ may lead to structural collapse or pore blockage, ultimately reducing the number of accessible adsorption sites (Lin et al., 2025).

3.3. Characteristic carbon structures for high porosity and thermal stability

To test the high-performance biochar samples, we initially observed their morphologies under SEM, and two optimal biochar samples exhibited a typically porous and sheet-like structure (Fig. 3A). Specifically, the Msa01 biochar displayed an open and loosely stacked lamellar architecture with a rough surface, abundant fissures and well-developed hierarchical porosity, which was likely attributed to the G-rich lignin precursor as the G-monomer contains one methoxy group that favors linear polymerization and rigid carbon sheet formation during carbonization. By contrast, the Msa24 biochar showed a denser surface with localized aggregation and particulate attachments responsible for fewer visible pores, which may be mainly due to its relatively high S- and H-monomer levels for a compact and less porous carbon matrix (Li and Shi, 2023). Despite identical $ZnCl_2$ activation conditions, the distinct monomeric proportions of the two Miscanthus accessions determined their carbonization pathways and microstructural evolution, resulting in two optimal biochar samples with different adsorption behaviors. For example, the open lamellar carbon structure of the Msa01 sample is favorable for small molecule diffusion, whereas the compact carbon matrix of Msa24 sample may enhance π–π stacking and hydrogen-bonding interactions with large-molecule dye. Randomized Raman spectroscopy across multiple regions showed that both biochar samples were of similar I_D/I_G ratios ranging from 0.68 to 0.74, with low coefficients of variation (3.4 %, 2.3 % CV) (Fig. 3B), indicating a uniform graphitic disorder across the carbon matrix. Nitrogen adsorption–desorption isotherms presented well-defined hysteresis loops indicative of mesoporous structures in two biochar samples (Fig. 3C). By comparison, the Msa01 biochar exhibited a higher specific surface area (1558.4 m^2/g) and smaller average pore size (2.30 nm), whereas the Msa24 biochar showed slightly lower surface area (1526.8 m^2/g) and larger average pore diameter (2.40 nm) with relatively increased total pore volume (0.915 cm^3/g) (Fig. 3D, Table 1). The results suggested that the Msa01 biochar may offer more active adsorption sites and the Msa24 biochar could accommodate large-molecule dye via facilitated diffusion. Thermal gravimetric analysis indicated that two biochar samples were of excellent thermal stability with carbon yields exceeding 79.0 % (Fig. 3E). Particularly, the Msa24 biochar had slightly higher residual mass (79.3 %), consistent with its more compact carbon structure

Table 1
BET apparent surface area and porosity of two optimal $ZnCl_2$-activated biochar samples.

Sample	Surface area (m2/g)	Pore Volume (cm3/g)			Pore Size (nm)
		Vtotal	Vmicro	Vmeso	
Msa01	1558.4	0.897	0.189	0.708	2.30
Msa24	1526.8	0.915	0.192	0.723	2.40

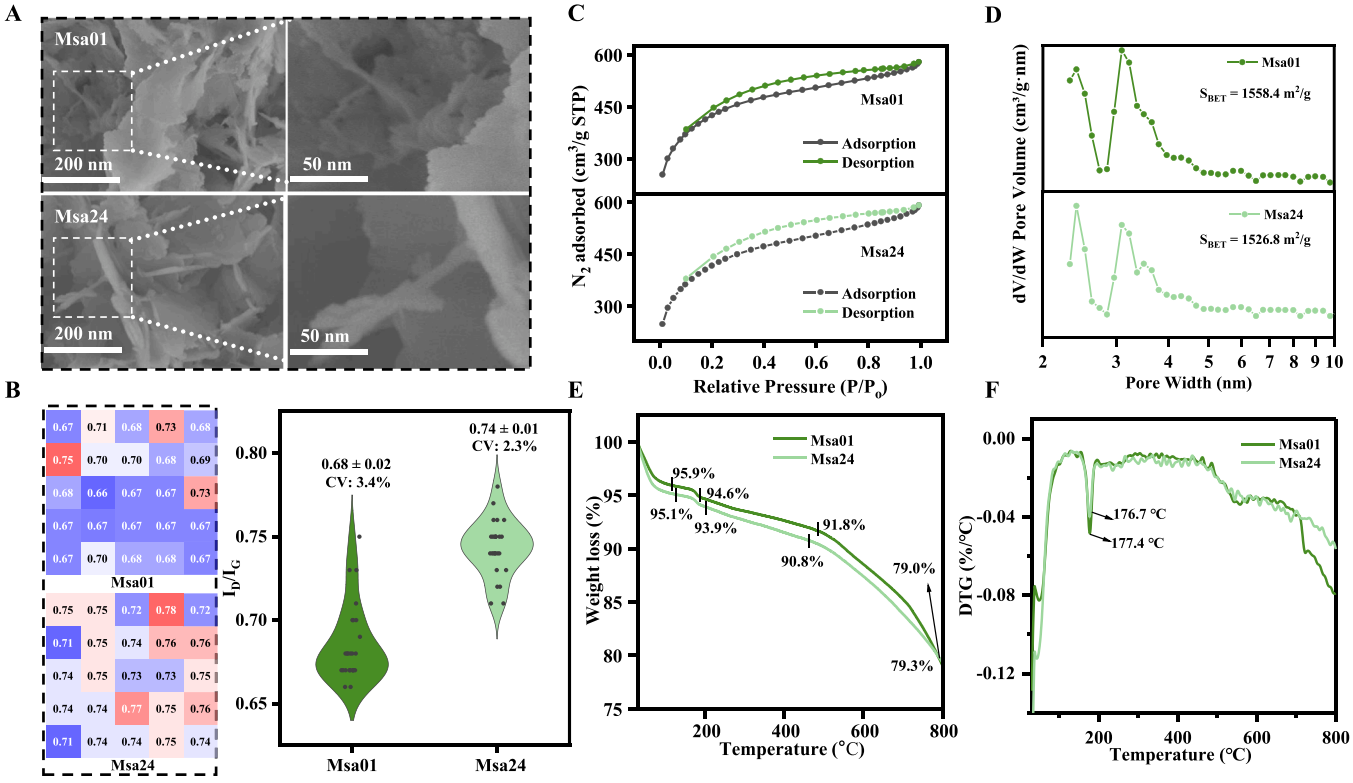

Fig. 3. Characterization of porosity and of thermal stability of the biochar samples as described in Fig. 2. (A) Scanning electron microscopy (SEM) images of two optimal biochar samples prepared by 400 ℃ and 1:2 lignin-$ZnCl_2$ ratio; (B) Raman spectra data collected from 25 randomly selected points within a representative area (4 × 4 mm) on the biochar surface, and corresponding I_D/I_G values calculated, CV as coefficient of variation; (C) N_2 adsorption–desorption isotherms; (D) Pore size distribution curves, S_{BET}: Surface area; (E, F) Thermogravimetric (TG) and derivative thermogravimetric (DTG) curves.

observed under SEM. The DTG curves further revealed that two biochar samples had the maximum weight loss rate near 177 °C, with Msa01 decreasing from 95.9 % to 94.6 % and Msa24 from 95.1 % to 93.9 % (Fig. 3F).

Moreover, the chemical composition and surface functionalities of the biochar samples characterized by elemental analysis and XPS profiling (Table 2). As a result, the Msa01 biochar had a slightly higher carbon content and lower oxygen content than the Msa24 did. The XPS spectra exhibited the presence of C, O, and Zn in both biochar samples, but the Msa24 sample had relatively higher O and Zn contents (Fig. 4), indicative of a more intense oxidative activation and Zn incorporation. High-resolution C 1 s spectra showed major peaks at 284.8 eV (C-C), 286.3 eV (C-O-C), and ~288.8 eV (O-C═O) (Fig. 4, Table S1), and the Msa24 biochar displayed a higher proportion of ether (C–O–C) linkages, likely due to $ZnCl_2$-mediated molecular rearrangement and condensation reactions. The O 1 s spectra showed strong C-O and O═C-O signals, confirming the enrichment of oxygenated functional groups (Fig. 4), and the Zn 2p spectra exhibited characteristic peaks at ~1022 eV (Zn $2p_{3/2}$) and ~1045 eV (Zn $2p_{1/2}$), corresponding to the Zn^{2+} species occurring in Zn-O bonding environments and residual $ZnCl_2$ (Fig. 4). It suggested that Zn^{2+} was partially embedded into the carbon matrix and potentially contributing to structural stabilization. In addition, the XRD patterns revealed diffraction signals corresponding to both ZnO (31.65°, 34.38°, 36.00°, 47.59°, 56.60°, 62.87°) and unreacted $ZnCl_2$ (27.0°) in two optimal biochar samples (Fig. 4, Fig. S7), indicating the incomplete transformation of $ZnCl_2$ during pyrolysis. These observations suggest that the activation process likely involved the following reactions:

$$\text{Lignin } (C_xH_yO_z) + ZnCl_2 + 3H_2O \rightarrow C_xH_{y-6}O_{z-3} + ZnOCl_2{\cdot}2H_2O + 2HCl \quad (8)$$

$$Zn_2OCl_2{\cdot}2H_2O \rightarrow ZnCl_2 + ZnO + 2H_2O \quad (9)$$

Importantly, these characterizations directly supported the proposed adsorption mechanisms: (1) The graphitic structure by XRD assay should facilitate π−π stacking interactions with aromatic dyes; (2) The oxygen-containing groups (C-O, C═O) identified by XPS analysis could not only act as electron donors for the reduction of heavy metal ions, but should also serve as active sites for hydrogen bonding with organic pollutants.

3.4. Selective maximum adsorption of two optimal biochar

To evaluate the adsorption performance, the two optimal biochar samples were applied to adsorb four distinct industrial pollutants (MB, RB, TC, and Cr(VI)) (Fig. 5A). Adsorption isotherms were conducted under varying initial concentrations (MB: 400–1200 mg/L; RB: 100–2500 mg/L; TC: 200–1000 mg/L; Cr: 100–500 mg/L). The results showed that the Msa01 biochar exhibited consistently higher MB adsorption capacities than the Msa24 did (Fig. 5B), whereas the Msa24 biochar had significantly higher RB adsorptions (Fig. 5C). Given that Msa01 biochar possessed smaller pore sizes and the Msa24 biochar consisted of a high proportion of mesopores, it should explain why the Msa01 biochar is more favorable for the adsorption with relatively-smaller-molecule MB (~1.43 nm) and the Msa24 biochar is more effective for large-molecule RB (2–3 nm). Furthermore, Langmuir, Freundlich, and Temkin isotherm models were applied to clarify two optimal biochar adsorptions with MB and RB (Fig. S8, Table 3). For MB and TC, the determination coefficients (R^2) of the Freundlich model were generally higher than those of the Langmuir model, suggesting that the adsorption primarily occurs on a heterogeneous surface involving multilayer adsorption. In terms of RB adsorption, the Msa01 sample followed the Freundlich model ($R^2 > 0.83$), whereas the Msa24 biochar exhibited a better fit to the Langmuir model ($R^2 = 0.989$), indicating monolayer coverage for this specific system. Moreover, the Msa01 biochar showed a higher affinity for the small-molecule MB (541.9 mg/g) and TC (731.9 mg/g), whereas the Msa24 biochar achieved a remarkably high capacity for the large-molecule RB (1286.1 mg/g), which was substantially higher than that of Msa01 (810.1 mg/g). The findings confirmed that Msa01 was more suitable for removing smaller pollutants, whereas Msa24 effectively accommodated larger dye molecules. For heavy metal Cr(VI) adsorption, both biochar samples demonstrated high removal efficiencies with capacities ranging from 381.2 mg/g to 392.1 mg/g (Fig. 5E, Table 4). As the exceptionally high specific surface areas (> 1500 m^2/g) could provide abundant active sites, the removal mechanism should be primarily governed by chemical interactions rather than simple pore filling. Specifically, the process involves the electrostatic attraction between the positively charged biochar surface and anionic Cr(VI). Because electron-rich functional groups on the biochar could reduce the highly toxic Cr(VI) to Cr(III), an adsorption-coupled reduction mechanism was likely involved. Furthermore, this study compared the adsorption performances of two optimal biochar samples with those of other biochar-based adsorbents as previously reported (Tables 4–7). (Ahmed et al., 2019; Chen et al., 2019; De Benedetto et al., 2020; Du et al., 2017; Fan et al., 2024b, 2025; Jahani et al., 2023; Ji, 2025; Jia et al., 2021; Li et al., 2024a; Liu et al., 2021b; Luo et al., 2023; Lv et al., 2020; Mbarki et al., 2022; Mei et al., 2021; Sun et al., 2022; Wang et al., 2025a, 2025b, 2025c; Xie et al., 2021; Zhang et al., 2021a, 2022; Zhao et al., 2020, 2024). Notably, both Msa01 and Msa24 biochar samples respectively achieved the highest adsorption capacities for MB/RB/TC/Cr(VI) among all biochar samples presented, which attributed to the larger surface areas of the two optimal biochar samples examined. More importantly, other biochar samples have been prepared under higher temperatures ranging from 500 °C to 900 °C, and only one biochar sample (derived from corncob lignin via $MnSO_4$ activation at 500 °C) exhibited a markedly lower MB adsorption capacity (Table 4). Thus, the two $ZnCl_2$-activated biochar samples at low temperature not only presented the highest dye adsorption capacities, but they also offered the advantages in terms of lower energy input and more selective dye removal. Overall, these findings highlight that the adsorption selectivity of biochar is strongly governed by their pore architecture, where narrower pore channels facilitate the uptake of small-molecule dyes (e.g., MB), larger pore size and volume enhance adsorption of large-molecule organics (e.g., RB and TC), and the combination of high surface area and pore volume contributes to the efficient removal of heavy metals (e.g., Cr(VI)).

Table 2
Elemental composition of two optimal $ZnCl_2$-activated biochar samples.

Sample	Weight percent (wt%)				
	C	H	O	N	S
Msa01	69.0	2.54	9.08	0.417	0.989
Msa24	66.9	2.41	10.5	0.383	0.775

3.5. Dye adsorption kinetics and interactive mechanism

Adsorption kinetics were analyzed to elucidate the dye adsorption rates and mechanisms of the two optimal biochar samples (Fig. 6). For MB adsorption, both biochar samples exhibited rapid adsorption behavior to reach the equilibrium within 120 min, with a distinct fast uptake phase in the first 20 min. The Msa01 biochar maintained a higher adsorption capacity than Msa24 did, consistent with the results described above. For RB adsorption, the biochar samples required a longer equilibrium time of 300 min, and the Msa24 biochar exhibited a greater uptake capacity, validating its superiority in adsorbing large-molecule dye. Kinetic data were fitted to pseudo-first-order, pseudo-second-order, and intraparticle diffusion models (Fig. 6B-E). The experimental data for MB and RB adsorption on both biochar samples fitted well with the pseudo-second-order models with high R^2 values (Table S2), suggesting that the adsorption rate was likely controlled by the availability of active sites rather than solely by diffusion (Fig. 6E, Table S3). The decreasing slope in each stage confirms the significance of intraparticle diffusion in governing the overall kinetics, consistent

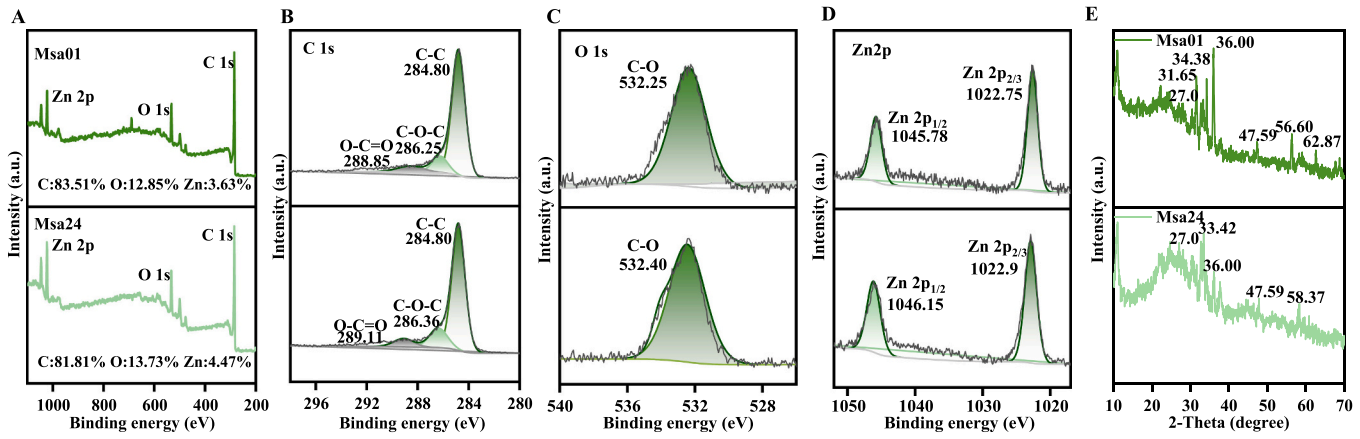

Fig. 4. Chemical properties of two optimal $ZnCl_2$-activated biochar samples. (A) Full XPS survey spectra; (B) High-resolution C 1 s spectra; (C) High-resolution O 1 s spectra; (D) High-resolution Zn 2p spectra; (E) XRD patterns.

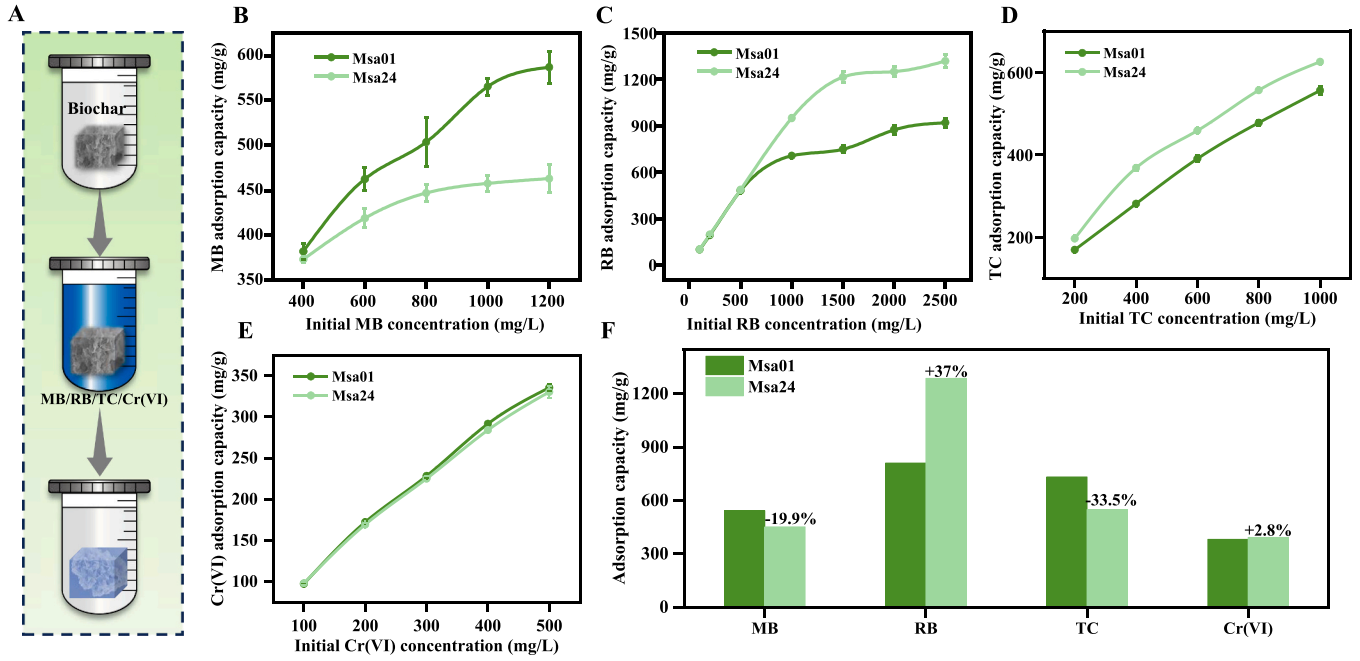

Fig. 5. Adsorption capacities of two optimal $ZnCl_2$-activated biochar samples with MB, RB, TC and Cr(VI). (A) Schematic illustration of adsorption process; (B, C, D, E) Adsorption capacities under initial concentrations of MB, RB, TC and Cr(VI); (F) Comparison of maximum adsorption capacities. Adsorption conditions: T = 25 °C, t = 6 h.

Table 3
Parameters of isothermal adsorption models of two optimal $ZnCl_2$-activated biochar samples.

Sample	Pollution	Langmuir			Freundlich			Temkin		
		q_{max} (mg/g)	b (L/mg)	R^2_{adj}	K_F	$1/n$	R^2_{adj}	b_t(J/mol)	k_t(L/mg)	R^2_{adj}
Msa01	MB	541.9	0.204	0.621	283.0	0.110	0.923	50.3	0.164	0.889
Msa24		451.1	0.357	0.788	322.0	0.055	0.982	109.3	1.250	0.975
Msa01	RB	810.1	0.171	0.748	270.5	0.162	0.835	27.8	0.010	0.825
Msa24		1286.1	0.136	0.989	417.0	0.172	0.803	15.3	0.005	0.896
Msa01	TC	731.9	0.006	0.941	31.8	0.471	0.996	17.3	-11.1	0.932
Msa24		548.4	0.168	0.739	176.8	0.209	0.972	32.7	4.98	0.943
Msa01	Cr(VI)	381.2	0.032	0.613	93.7	0.238	0.895	30.4	-0.001	0.920
Msa24		392.1	0.024	0.597	88.1	0.244	0.879	28.6	-0.003	0.931

with a multi-step adsorption mechanism. Fourier-transform infrared spectroscopy was employed to identify the changes in functional groups after dye adsorption (Fig. 6E-H). Prior to adsorption, both Msa01 and Msa24 biochar samples displayed characteristic peaks corresponding to C═C (1576 cm^{-1}), C-O (1159 cm^{-1}), C-C (878 cm^{-1}), and C-H (712 cm^{-1}) bonds. After MB adsorption, new peaks appeared to correspond for MB interactions to C═N (1540 cm^{-1}), C-N (1019 cm^{-1}), and C-S (731 cm^{-1}). These peaks are characteristic of the MB molecule structure and account

Table 4
Comparison of MB adsorption capacities among biochar samples prepared in this study and previously reported.

Sample	Activating agent	Temperature(℃)	S_{BET} (m^2/g)	MB adsorption capacity (mg/g)	Reference
Msa01-lignin	**$ZnCl_2$**	**400**	**1558.4**	**541.9**	**This work**
Straw powder	$(NH_4)_3PO_4$	900	368.0	156.4	Fan et al. (2025)
Sorghum straw	$FeCl_3$	600	268.1	156.4	Xie et al. (2021)
Corn stigma	H_3PO_4	500	820.0	330.5	Mbarki et al. (2022)
corncob residue-Lignin	$MnSO_4$	400	547.2	249.0	Liu et al. (2021b)
seaweed	/	800	926.4	512.7	Ahmed et al. (2019)
Technical lignin	$FeCl_3$·6 H_2O	800	886.0	448.4	Sun et al. (2022)
paper-shelled almonds	$ZnCl_2$	500	1100.0	430.0	Wang et al. (2025a)

Table 5
Comparison of RB adsorption capacities among biochar samples prepared in this study and previously reported.

Sample	Activating agent	Temperature (℃)	S_{BET} (m^2/g)	RB adsorption capacity (mg/g)	Reference
Msa24-lignin	**$ZnCl_2$**	**400**	**1526.8**	**1286.1**	**This work**
@3Xylan	/	600	317.0	107.5	Wang et al. (2025b)
Nanotube	/	/	108.7	33.0	De Benedetto et al. (2020)
traditional Chinese medical residual	$Mg(OH)_2$	900	681.4	103.1	Zhang et al. 2022c
Rice husk	Sludge	500	29.2	38.5	Chen et al. (2019)
powdered activated carbon	$Ca(NO_3)_2$·4 H_2O	600	1261.7	660.5	Lv et al. (2020)
Milkvetch plant	ZnO-Ce	500	636.5	5.81	Jahani et al. (2023)
MNS	KOH	/	876.8	376.8	Du et al. (2017)

for its adsorption onto the biochar surface, revealing a strong chemical interaction between MB and biochar surface. Similarly, the RB adsorption exhibited the additional C-N and C-S bands, further verifying the presence of adsorbed dye. Besides new covalent bond formation, the spectral changes combined with molecular dynamics analysis should support a mechanism model driven by strong pollutant–surface interactions such as electrostatic and π−π interactions.

3.6. Molecular dynamics simulation for adsorption mechanism

Based on the elemental composition data (Table 2), this study performed molecular dynamics simulations to construct molecular structure models of the two optimal biochar samples responsible for dye adsorption (Fig. 7; Fig. S9). The simulation data revealed that the Msa01 biochar exhibited a high interaction energy with MB at −416.4 kJ/mol, which was approximately 9.2 % stronger than that of the Msa24 biochar (Fig. 7B & C). Importantly, these high energy magnitudes represent the cumulative sum of non-covalent interactions (Van der Waals and electrostatic forces) across the entire contact interface of the planar dye molecules, rather than the formation of covalent bonds. However, the values were higher in magnitude than the experimental ones, mainly due to the exclusion of desolvation energy penalties in the simulations. In addition, the Msa24 biochar displayed a remarkably strong interaction with RB (-480.9 kJ/mol), being consistent with its superior experimental adsorption capacity. This also re-validated the Msa24 biochar rich at surface oxygen with a compact structure, which should facilitate π–π interactions and hydrogen bonding with the conjugated RB molecules. The findings were thus consistent with the experimental adsorption data obtained above, and further elucidated the dynamic relationships among the biochar morphology, surface functionality, and molecular-level adsorption behavior.

3.7. Reusable $ZnCl_2$-activation agent and recyclable biochar

For the sustainability and practical applicability, this study examined the reuse of activating agent ($ZnCl_2$) and the recycling performance of the biochar adsorbents (Fig. 8A). In terms of agent reuse, $ZnCl_2$ was recovered after use and re-applied in successive rounds of biochar preparation for MB and RB adsorption (Fig. 8B & C). The Msa01 biochar samples exhibited an initial MB adsorption capacity of 585.8 mg/g and a retained capacity of 298.7 mg/g after the third cycle, which was consistently higher than those of the Msa24 samples. Conversely, the Msa24 biochar samples remained higher RB adsorption capacities than Msa01, suggesting that the reused-$ZnCl_2$ activations may not substantially alter the biochar structures from the lignin substrates of the two *Miscanthus* accessions. The reduced adsorption performance over cycles was mainly attributed to the partial loss of $ZnCl_2$ during repeated activation. Meanwhile, this study evaluated the recyclability of the biochar adsorbents by performing five consecutive adsorption–desorption cycles (Fig. 8D & E). Notably, all biochar samples exhibited only a slightly reduced RB adsorption capacity over five cycles, and the Msa24 biochar samples maintained 97.4 % of its initial RB adsorption capacity (494 mg/g), indicating that the $ZnCl_2$-activated biochar samples possessed outstanding stability and recyclability for large-molecule dye adsorption (Fig. 8E). On the other hand, the $ZnCl_2$-activated biochar samples showed a relatively large reduction in MB adsorption capacities (Fig. 8D). This decline was likely due to the incomplete desorption of the dye molecules. Specifically, the smaller MB molecules could deeply penetrate into the internal tortuous mesoporous channels (pore trapping), causing partial pore blockage and making them difficult to fully

Table 6
Comparison of TC adsorption capacities among biochar samples prepared in this study and previously reported.

Sample	Activating agent	Temperature(℃)	S_{BET} (m^2/g)	TC adsorption capacity (mg/g)	Reference
Msa01-lignin	**$ZnCl_2$**	**400**	**1558.4**	**731.9**	**This work**
crayfish shell	ball-mill	800	289.7	60.7	Zhang et al. (2021a)
rice husk	$Bi_2O_2CO_3$	500	22.7	173.0	Luo et al. (2023)
Rice straw	$FeCl_3$·6 H_2O and urea	700	606.6	156.0	Mei et al. (2021)
biogas residue	ball-mill	700	412.0	289.1	Fan et al. (2024b)
reed	KOH	650	965.3	173.6	Zhao et al. (2020)
Cow dung	$KMnO_4$ and KOH	700	231.6	142.6	Wang et al. (2025c)

Table 7
Comparison of Cr(VI) adsorption capacities among biochar samples prepared in this study and previously reported.

Sample	Activating agent	Temperature(℃)	S_{BET} (m^2/g)	Cr(VI) adsorption capacity (mg/g)	Reference
Msa24-lignin	**$ZnCl_2$**	**400**	**1526.8**	**392.1**	**This work**
sesame straw	$FeCl_3$·6 H_2O	550	/	12.6	Li et al. (2024a)
badam shell	H_3PO_4	550	1359.5	276.6	Jia et al. (2021)
Fe-containing sludge	$(NH_4)_2S_2O$	700	89.5	167.5	Ji et al. 2025
groundnut shell	/	350	13.4	142.9	Shakya et al. 2022
banana straw	$MgCl_2$	430	36.4	125.0	Li et al. 2020a
sludge	$KHCO_3$	700	295.8	41.2	Zhao et al. (2024)

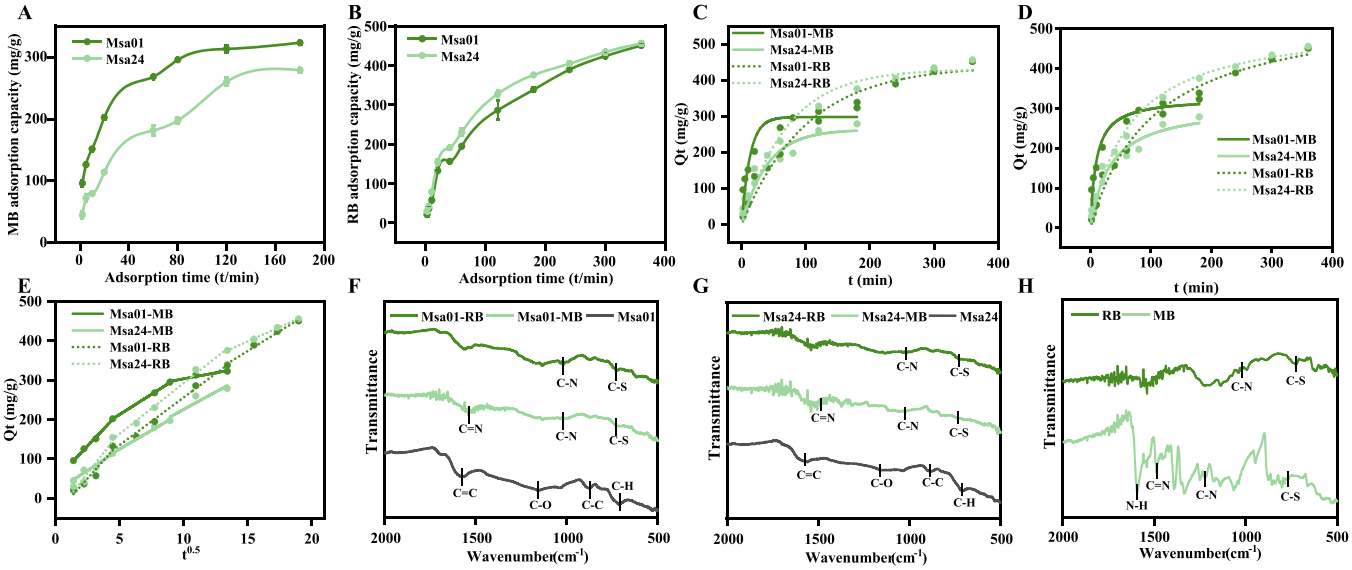

Fig. 6. Optimal MB and RB adsorption capacities of two optimal $ZnCl_2$-activated biochar samples. (A, B) Adsorption capacities of MB and RB under a time course; (C) Pseudo-first-order kinetic model for dye adsorption; (D) Pseudo-second-order kinetic model; (E) Intraparticle diffusion model; (F, G) Fourier transform infrared (FTIR) spectra of biochar (Msa01, Msa24) before and after dye adsorption; (H) FTIR spectra of biochar adsorbed with dyes. Adsorption conditions: T = 25°C, t = 6 h, C_{MB} = 400 mg/L, C_{RB} = 500 mg/L.

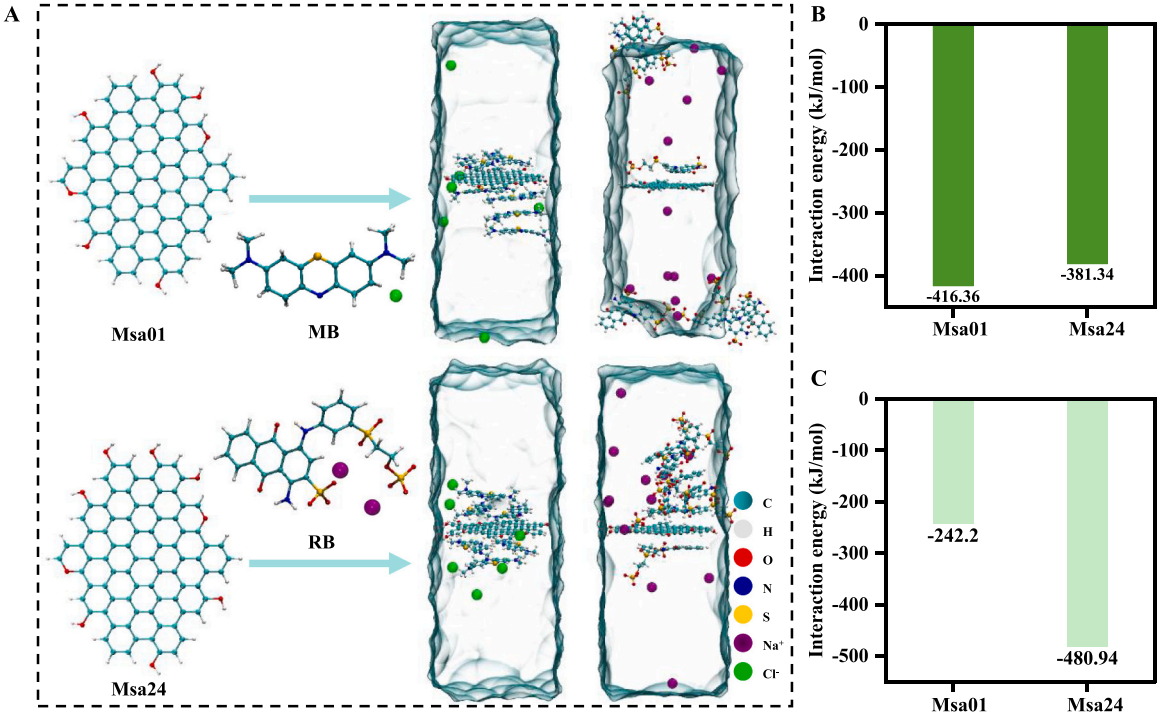

Fig. 7. Dynamics simulation model of biochar interactions with MB and RB dyes. (A) Adsorption process with dyes; (B) Interaction energy (E_{int}) with MB; (C) Interaction energy (E_{int}) with RB.

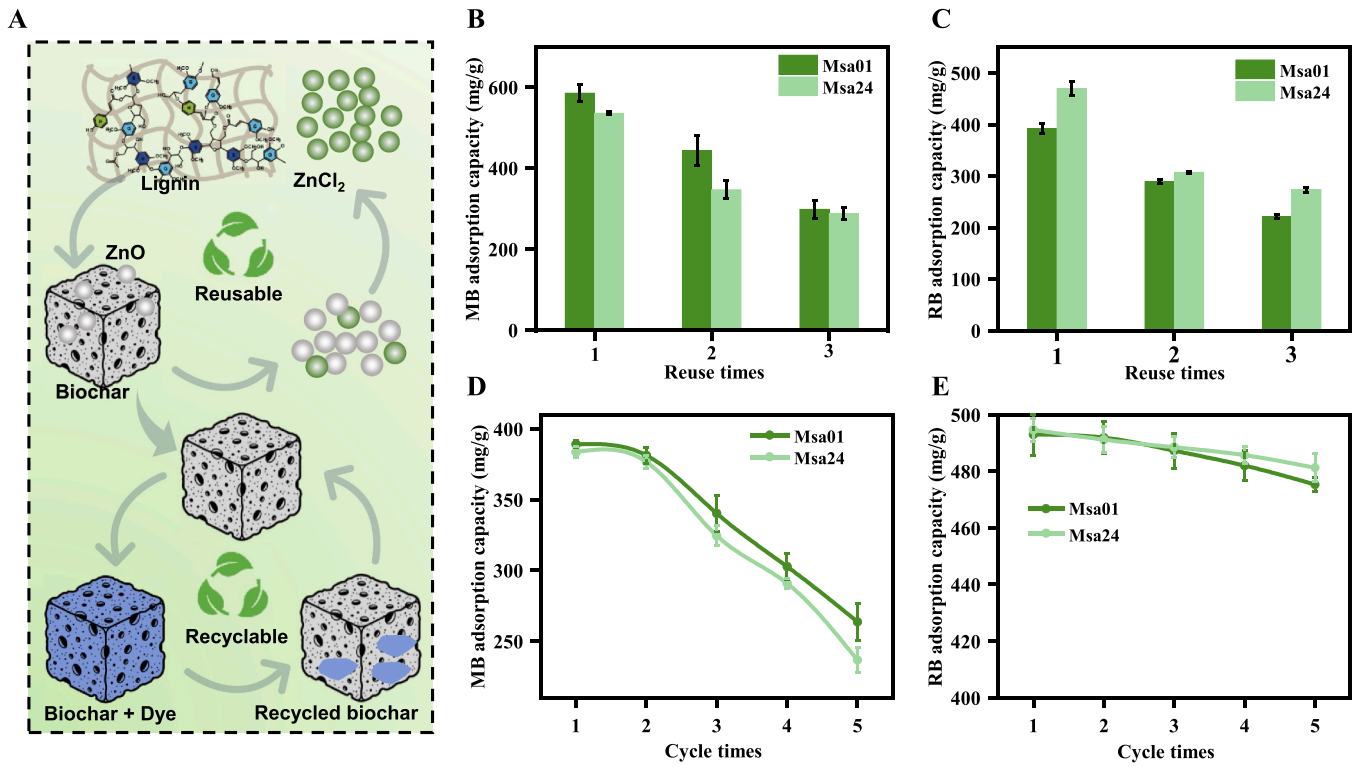

Fig. 8. Regeneration performance of $ZnCl_2$ activation agent and biochar adsorbent. (A) Schematic illustration of activation and biochar regeneration; (B, C) $ZnCl_2$ adsorption cycles for MB (A) and RB (B); (D, E) Recycling performance of biochar for MB (C) and RB (D). Adsorption conditions: (B, C) T = 25°C, t = 6 h, C_{MB} = 1 g/L, C_{RB} = 500 mg/L; (D, E) T = 25°C, t = 6 h, C_{MB} = 400 mg/L, C_{RB} = 500 mg/L.

elute. Therefore, both the $ZnCl_2$ activation agent and the biochar were highly reusable and recyclable for dye adsorption.

4. Conclusion

Two optimal hierarchical porous biochar samples were prepared via low-temperature (400 °C) $ZnCl_2$ activation with the alkali-extracted lignin substrates of two *Miscanthus* accessions distinguished by G- and H-monomer proportions. This thermochemical conversion offered significant advantages over biomass-derived biochar materials as previously generated using other chemical activators under much higher temperatures. Notably, the two optimal biochar samples exhibited exceptionally large specific surface areas with distinct pore structures, enabling pollutant-selective adsorption: efficient uptake of small-molecule dyes (e.g., MB), superior removal of larger organics including RB and TC, and strong adsorption of heavy metals (e.g., Cr (VI)). Adsorption isotherm and kinetic analyses, supported by molecular dynamics simulations, revealed a predominant monolayer adsorption mechanism accompanied by durable pollutant–surface interactions. In addition, this study highlighted that $ZnCl_2$ was reusable as activation agent and the biochar was highly recyclable as an active adsorbent particularly for high-capacity RB adsorption. Therefore, this study has demonstrated a sustainable route for valorizing lignin-rich agricultural and forestry residues into advanced carbon materials with tunable selectivity, offering practical potential for the removal of both organic and inorganic contaminants from wastewater.

CRediT authorship contribution statement

Junsheng Yu: Writing – original draft, Visualization, Software, Methodology, Investigation. **Zongtai Tang**: Writing – original draft, Software, Methodology, Investigation. **Lei Zhu**: Writing – original draft, Software, Methodology, Investigation. **Bing Gao**: Writing – original draft, Software, Methodology, Investigation. **Jing Hong**: Writing – original draft, Software, Methodology, Investigation. **Yujia Fang**: Writing – original draft, Software, Methodology, Investigation. **Jiacheng Kang**: Writing – original draft, Software, Methodology, Investigation. **Hao Peng**: Writing – review & editing, Investigation. **Dan Sun**: Writing – review & editing, Investigation. **Boyang He**: Software, Methodology, Investigation. **Bakr Mahmoud M. A.**: Software, Methodology, Investigation. **Yanting Wang**: Writing – review & editing, Funding acquisition. **Liangcai Peng**: Writing – review & editing, Supervision, Funding acquisition, Conceptualization. **Hua Yu**: Writing – review & editing, Supervision, Methodology, Funding acquisition.

Declaration of Competing Interest

The authors declare that they have no known competing financial interests or personal relationships that could have appeared to influence the work reported in this paper.

Acknowledgements

This work was supported by the National Natural Science Foundation of China (32500325, 3247027, 32170268), Hubei Provincial Natural Science Foundation of China for Excellent Young Scientists (2024AFA100), the Doctoral Research Start-up Fund of Hubei University of Technology (XJ2024000402), the Initiative Grant of Hubei University of Technology for High-level Talents (GCC20230001).

Appendix A. Supporting information

Supplementary data associated with this article can be found in the online version at doi:10.1016/j.indcrop.2026.122630.

Data availability

The data that has been used is confidential.

References

Abraham, M.J., Murtola, T., Schulz, R., Páll, S., Smith, J.C., Hess, B., Lindahl, E., 2015. GROMACS: high performance molecular simulations through multi-level parallelism from laptops to supercomputers. SoftwareX 1-2, 19–25. https://doi.org/10.1016/j.softx.2015.06.001.

Ahmed, M.J., Okoye, P.U., Hummadi, E.H., Hameed, B.H., 2019. High-performance porous biochar from the pyrolysis of natural and renewable seaweed (*Gelidiella acerosa*) and its application for the adsorption of methylene blue. Bioresour. Technol. 278, 159–164. https://doi.org/10.1016/j.biortech.2019.01.054.

Ai, Y., Wang, H., Liu, P., Yu, H., Sun, M., Zhang, R., Tang, J., Wang, Y., Feng, S., Peng, L., 2024. Insights into contrastive cellulose nanofibrils assembly and nanocrystals catalysis from dual regulations of plant cell walls. Sci. Bull. 69 (24), 3815–3819. https://doi.org/10.1016/j.scib.2024.06.013.

Ali, M., Mahmood, F., Magoua Mbeugang, C.F., Tang, J., Xie, X., Li, B., 2025. Molten chloride salt pyrolysis of biomass: Effects of temperature and mass ratio of molten salt to biomass. Energy 316, 134634. https://doi.org/10.1016/j.energy.2025.134634.

An, Q., Sun, J., Yang, J., Yuetikuer, A., Zhang, S., Leng, L., Zhan, H., 2025. Thermochemical valorization of tobacco wastes into biofuels and carbon materials: a comprehensive review. Chem. Eng. J. 505, 159544. https://doi.org/10.1016/j.cej.2025.159544.

Berendsen, H., Postma, J.P.M., van Gunsteren, W., DiNola, A.D., Haak, J.R., 1984. Molecular-dynamics with coupling to an external bath. J. Chem. Phys. 81, 3684. https://doi.org/10.1063/1.448118.

Bergna, D., Varila, T., Romar, H., Lassi, U., 2022. Activated carbon from hydrolysis lignin: Effect of activation method on carbon properties. Biomass.. Bioenerg. 159, 106387. https://doi.org/10.1016/j.biombioe.2022.106387.

Bussi, G., Donadio, D., Parrinello, M., 2007. Canonical sampling through velocity rescaling. J. Chem. Phys. 126 (1), 014101. https://doi.org/10.1063/1.2408420.

Chen, S., Qin, C., Wang, T., Chen, F., Li, X., Hou, H., Zhou, M., 2019. Study on the adsorption of dyestuffs with different properties by sludge-rice husk biochar: adsorption capacity, isotherm, kinetic, thermodynamics and mechanism. J. Mol. Liq. 285, 62–74. https://doi.org/10.1016/j.molliq.2019.04.035.

Cheng, S., Yu, H., Hu, M., Wu, Y., Cheng, L., Cai, Q., Tu, Y., Xia, T., Peng, L., 2018. *Miscanthus* accessions distinctively accumulate cadmium for largely enhanced biomass enzymatic saccharification by increasing hemicellulose and pectin and reducing cellulose CrI and DP. Bioresour. Technol. 263, 67–74. https://doi.org/10.1016/j.biortech.2018.04.031.

De Benedetto, C., Macario, A., Siciliano, C., B. Nagy, J., De Luca, P., 2020. Adsorption of reactive blue 116 dye and reactive yellow 81 dye from aqueous solutions by Multi-walled carbon nanotubes. Materials 13 (12), 2757. https://doi.org/10.3390/ma13122757.

De Smedt, J., Arauzo, P.J., Ronsse, F., 2025. Assessing the reusability of activating agents during molten salt activation of pinewood. J. Environ. Chem. Eng. 13 (2), 116050. https://doi.org/10.1016/j.jece.2025.116050.

Du, C., Xue, Y., Wu, Z., Wu, Z., 2017. Microwave-assisted one-step preparation of macadamia nut shell-based activated carbon for efficient adsorption of reactive blue. N. J. Chem. 41 (24), 15373–15383. https://doi.org/10.1039/C7NJ03208K.

Egun, I.L., Akinwolemiwa, B., He, H., Ma, M., Chen, Z., Chen, G.Z., Hu, D., 2025. Molten base carbonisation and activation of non-lignin-rich biomass into hierarchically porous carbon with surface-rich functionalities for supercapacitor electrodes. Chem. Eng. J. 509, 161386. https://doi.org/10.1016/j.cej.2025.161386.

Fan, M., Shao, Y., Wang, Y., Sun, J., He, H., Jiang, Y., Zhang, S., Wang, Y., Hu, X., 2024a. Preparation of activated carbon with recycled $ZnCl_2$ for maximizing utilization efficiency of the activating agent and minimizing generation of liquid waste. Chem. Eng. J. 500, 157278. https://doi.org/10.1016/j.cej.2024.157278.

Fan, S., Zhang, W., Fan, X., Wang, S., Fang, X., Zhou, N., Xu, H., 2024b. Hydrothermal pretreatment and pyrolytic conversion of biogas residue into biochar for efficient adsorption of tetracycline. Fuel 358, 130244. https://doi.org/10.1016/j.fuel.2023.130244.

Fan, S., Zhao, M., Luo, J., Li, W., Fan, X., Zhou, N., Xu, H., Shi, Y., 2025. Facile preparation of N/P co-doped mesoporous biochar for efficient removal of methylene blue from aqueous solutions: A 2D-FTIR-COS, adsorption mechanism analysis, and fixed-bed column study. J. Water Process Eng. 72, 107479. https://doi.org/10.1016/j.jwpe.2025.107479.

Fu, Y., Gao, H., Yu, H., Yang, Q., Peng, H., Liu, P., Li, Y., Hu, Z., Zhang, R., Li, J., Qi, Z., Wang, L., Peng, L., Wang, Y., 2022. Specific lignin and cellulose depolymerization of sugarcane bagasse for maximum bioethanol production under optimal chemical fertilizer pretreatment with hemicellulose retention and liquid recycling. Renew. Energ. 200, 1371–1381. https://doi.org/10.1016/j.renene.2022.10.049.

Han, H., Yin, W., Yang, B., Wang, D., Yao, J., Zhu, Z., 2022. Adsorption behavior of sodium oleate on iron minerals and its effect on flotation kinetics. Colloid Surf. A 647, 129108. https://doi.org/10.1016/j.colsurfa.2022.129108.

He, B., Hao, B., Yu, H., Tu, F., Wei, X., Xiong, K., Zeng, Y., Zeng, H., Liu, P., Tu, Y., Wang, Y., Kang, H., Peng, L., Xia, T., 2022. Double integrating *XYL2* into engineered *Saccharomyces cerevisiae* strains for consistently enhanced bioethanol production by effective xylose and hexose co-consumption of steam-exploded lignocellulose in bioenergy crops. Renew. Energ. 186, 341–349. https://doi.org/10.1016/j.renene.2021.12.103.

Hess, B., Bekker, H., Berendsen, H.J.C., Fraaije, J.G.E.M., 1997. LINCS: A linear constraint solver for molecular simulations. J. Comput. Chem. 18 (12), 1463–1472. https://doi.org/10.1002/(SICI)1096-987X(199709)18:12.

Hu, Z., Li, Q., Chen, Y., Li, T., Wang, Y., Zhang, R., Peng, H., Wang, H., Wang, Y., Tang, J., Nauman Aftab, M., Peng, L., 2023. Intermittent ultrasound retains cellulases unlock for enhanced cellulosic ethanol with high-porosity biochar for dye adsorption using desirable rice mutant straw. Bioresour. Technol. 369, 128437. https://doi.org/10.1016/j.biortech.2022.128437.

Humphrey, W., Dalke, A., Schulten, K., 1996. VMD: Visual molecular dynamics. J. Mol. Graph 14 (1), 33–38. https://doi.org/10.1016/0263-7855(96)00018-5.

Jahani, F., Maleki, B., Mansouri, M., Noorimotlagh, Z., Mirzaee, S.A., 2023. Enhanced photocatalytic performance of milkvetch-derived biochar via ZnO–Ce nanoparticle decoration for reactive blue 19 dye removal. Sci. Rep. 13 (1), 17824. https://doi.org/10.1038/s41598-023-45145-9.

Ji, Y., 2025. Adsorption performance of Cr(VI) using Fe-containing sludge biochar co-doped with nitrogen and sulfur. Biomass.. Convers. Bior 15 (14), 21507–21522. https://doi.org/10.1007/s13399-025-06712-4.

Jia, X., Zhang, Y., He, Z., Chang, F., Zhang, H., Wågberg, T., Hu, G., 2021. Mesopore-rich badam-shell biochar for efficient adsorption of Cr(VI) from aqueous solution. J. Environ. Chem. Eng. 9 (4), 105634. https://doi.org/10.1016/j.jece.2021.105634.

Laishram, D., Kim, S.-B., Lee, S.-Y., Park, S.-J., 2025. Advancements in biochar as a sustainable adsorbent for water pollution mitigation. Adv. Sci. 12 (19), 2410383. https://doi.org/10.1002/advs.202410383.

Li, H., Yu, L., Chen, Z., Xiao, B., Jin, K., 2024a. The characteristics of adsorption Cr(VI) by iron-modified and iron-doped phosphorus-based biochar biochar. Green. Chem. Lett. Rev. 17 (1), 2329607. https://doi.org/10.1080/17518253.2024.2329607.

Li, J., Bai, X., Fang, Y., Chen, Y., Wang, X., Chen, H., Yang, H., 2020. Comprehensive mechanism of initial stage for lignin pyrolysis. Combust. Flame 215, 1–9. https://doi.org/10.1016/j.combustflame.2020.01.016.

Li, M., Si, S., Hao, B., Zha, Y., Wan, C., Hong, S., Kang, Y., Jia, J., Zhang, J., Li, M., Zhao, C., Tu, Y., Zhou, S., Peng, L., 2014. Mild alkali-pretreatment effectively extracts guaiacyl-rich lignin for high lignocellulose digestibility coupled with largely diminishing yeast fermentation inhibitors in *Miscanthus*. Bioresour. Technol. 169, 447–454. https://doi.org/10.1016/j.biortech.2014.07.017.

Li, W., Shi, J., 2023. Lignin-derived carbon material for electrochemical energy storage applications: Insight into the process-structure-properties-performance correlations. Front Bioeng. Biotech. 11 - 2023. https://doi.org/10.3389/fbioe.2023.1121027.

Li, X., Liao, H., Fan, C., Hu, H., Li, Y., Li, J., Yi, Z., Cai, X., Peng, L., Tu, Y., 2016. Distinct geographical distribution of the *Miscanthus* accessions with varied biomass enzymatic saccharification. PLoS One 11 (8), e0160026. https://doi.org/10.1371/journal.pone.0160026.

Li, X., Cen, K., Li, J., Wang, C., Jia, D., Chen, D., 2024b. Effects of co-pyrolysis interaction performance of cellulose and lignin on the gas products and hydrogen generation path. Ind. Crop Prod. 222, 119858. https://doi.org/10.1016/j.indcrop.2024.119858.

Li, Y., He, B., Zhang, H., Liu, J., Li, S., Wang, H., Peng, H., Wang, Y., Dai, J., Wang, Y., Peng, L., Kang, H., 2024c. Enriched extensin and cellulose for non-collapse biochar assembly to maximize carbon porosity and dye adsorption with high bioethanol production. Ind. Crop Prod. 222, 119924. https://doi.org/10.1016/j.indcrop.2024.119924.

Lima, E.C., Hosseini-Bandegharaei, A., Moreno-Piraján, J.C., Anastopoulos, I., 2019. A critical review of the estimation of the thermodynamic parameters on adsorption equilibria. Wrong use of equilibrium constant in the Van't Hoof equation for calculation of thermodynamic parameters of adsorption. J. Mol. Liq. 273, 425–434. https://doi.org/10.1016/j.molliq.2018.10.048.

Lima, E.C., Sher, F., Guleria, A., Saeb, M.R., Anastopoulos, I., Tran, H.N., Hosseini-Bandegharaei, A., 2021. Is one performing the treatment data of adsorption kinetics correctly? J. Environ. Chem. Eng. 9 (2), 104813. https://doi.org/10.1016/j.jece.2020.104813.

Lin, R., Liu, R., Wang, L., Wang, Y., Zhu, N., Chen, D., Zhang, L., 2025. Effects of B-doping on the physicochemical structure and CO_2 adsorption property of the walnut shell bio-char. J. Anal. Appl. Pyrol 189, 107114. https://doi.org/10.1016/j.jaap.2025.107114.

Liu, J., Zhang, X., Peng, H., Li, T., Liu, P., Gao, H., Wang, Y., Tang, J., Li, Q., Qi, Z., Peng, L., Xia, T., 2023. Full-Chain $FeCl_3$ catalyzation is sufficient to boost cellulase secretion and cellulosic ethanol along with valorized supercapacitor and biosorbent using desirable corn stalk. Molecules 28 (5), 2060. https://doi.org/10.3390/molecules28052060.

Liu, P., Li, A., Wang, Y., Cai, Q., Yu, H., Li, Y., Peng, H., Li, Q., Wang, Y., Wei, X., Zhang, R., Tu, Y., Xia, T., Peng, L., 2021a. Distinct *Miscanthus* lignocellulose improves fungus secreting cellulases and xylanases for consistently enhanced biomass saccharification of diverse bioenergy crops. Renew. Energ. 174, 799–809. https://doi.org/10.1016/j.renene.2021.04.107.

Liu, X.-J., Li, M.-F., Singh, S.K., 2021b. Manganese-modified lignin biochar as adsorbent for removal of methylene blue. J. Mater. Res Techno 12, 1434–1445. https://doi.org/10.1016/j.jmrt.2021.03.076.

Liu, Y., Liu, Y.-J., 2008. Biosorption isotherms, kinetics and thermodynamics. Sep Purif. Technol. 61 (3), 229–242. https://doi.org/10.1016/j.seppur.2007.10.002.

Luo, Y., Zheng, A., Li, J., Han, Y., Xue, M., Zhang, L., Yin, Z., Xie, C., Chen, Z., Ji, L., Hong, Z., Xie, X., 2023. Integrated adsorption and photodegradation of tetracycline by bismuth oxycarbonate/biochar nanocomposites. Chem. Eng. J. 457, 141228. https://doi.org/10.1016/j.cej.2022.141228.

Lv, S., Zhou, Z., Xue, M., Zhang, X., Yang, Z., 2020. Adsorption characteristics of reactive blue 81 by powdered activated carbon: Role of the calcium content. J. Water Process Eng. 36, 101247. https://doi.org/10.1016/j.jwpe.2020.101247.

Mark, P., Nilsson, L., 2001. Structure and dynamics of the TIP3P, SPC, and SPC/E water models at 298 K. J. Phys. Chem. A 105 (43), 9954–9960. https://doi.org/10.1016/10.1021/jp003020w.

Mbarki, F., Selmi, T., Kesraoui, A., Seffen, M., 2022. Low-cost activated carbon preparation from Corn stigmata fibers chemically activated using H_3PO_4, $ZnCl_2$ and KOH: Study of methylene blue adsorption, stochastic isotherm and fractal kinetic. Ind. Crop Prod. 178, 114546. https://doi.org/10.1016/j.indcrop.2022.114546.

Mei, Y., Xu, J., Zhang, Y., Li, B., Fan, S., Xu, H., 2021. Effect of Fe–N modification on the properties of biochars and their adsorption behavior on tetracycline removal from aqueous solution. Bioresour. Technol. 325, 124732. https://doi.org/10.1016/j.biortech.2021.124732.

Memetova, A., Tyagi, I., Singh, L., Karri, R.R., Suhas, Tyagi, K., Kumar, V., Memetov, N., Zelenin, A., Tkachev, A., Bogoslovskiy, V., Shigabaeva, G., Galunin, E., Mubarak, N. M., Agarwal, S., 2022. Nanoporous carbon materials as a sustainable alternative for the remediation of toxic impurities and environmental contaminants: A review. Sci. Total Environ. 838, 155943. https://doi.org/10.1016/j.scitotenv.2022.155943.

Mutabazi, E., Qiu, X., Song, Y., Li, C., Jia, X., Hakizimana, I., Niu, J., Nuramkhaan, M., Zhao, Y., 2024. Cr(VI) adsorption on activated carbon, sludge derived biochar, and peanut shells derived biochar: Performance, mechanisms during the reuse process and site energy distribution analysis. J. Water Process Eng. 57, 104679. https://doi.org/10.1016/j.jwpe.2023.104679.

Patel, D., Singh, A., Ambati, S.R., Singh, R.S., Sonwani, R.K., 2024. An overview of recent advances in treatment of complex dye-containing wastewater and its techno-economic assessment. J. Environ. Manag. 370, 122804. https://doi.org/10.1016/j.jenvman.2024.122804.

Saha, N., Xin, D., Chiu, P.C., Reza, M.T., 2019. Effect of pyrolysis temperature on acidic oxygen-containing functional groups and electron storage capacities of pyrolyzed hydrochars. ACS Sustain. Chem. Eng. 7 (9), 8387–8396. https://doi.org/10.1021/acssuschemeng.9b00024.

Serra-Parareda, F., Tarrés, Q., Espinach, F.X., Vilaseca, F., Mutjé, P., Delgado-Aguilar, M., 2020. Influence of lignin content on the intrinsic modulus of natural fibers and on the stiffness of composite materials. Int J. Biol. Macromol. 155, 81–90. https://doi.org/10.1016/j.ijbiomac.2020.03.160.

Singh, P., Maiti, A., 2024. Optimized synthesis and characterization of laterite biochar composite for arsenic removal: examining colloidal stability and As(III) oxidation. Biochar 6 (1), 100. https://doi.org/10.1007/s42773-024-00389-0.

Sun, D., Alam, A., Tu, Y., Zhou, S., Wang, Y., Xia, T., Huang, J., Li, Y., Zahoor, Wei, X., Hao, B., Peng, L., 2017. Steam-exploded biomass saccharification is predominately affected by lignocellulose porosity and largely enhanced by Tween-80 in *Miscanthus*. Bioresour. Technol. 239, 74–81. https://doi.org/10.1016/j.biortech.2017.04.114.

Sun, Y., Wang, T., Han, C., Lv, X., Bai, L., Sun, X., Zhang, P., 2022. Facile synthesis of Fe-modified lignin-based biochar for ultra-fast adsorption of methylene blue: Selective adsorption and mechanism studies. Bioresour. Technol. 344, 126186. https://doi.org/10.1016/j.biortech.2021.126186.

Wang, D., Wang, X., Song, S., Hu, K., Wu, J., Chen, Y., 2025a. $ZnCl_2$-modified almond shell-based biochar for highly efficient adsorption of crystal violet and methylene blue in water. Biomass. Convers. Bior. https://doi.org/10.1007/s13399-025-06739-7.

Wang, H., Wang, X., Cui, Y., Xue, Z., Ba, Y., 2018. Slow pyrolysis polygeneration of bamboo (*Phyllostachys pubescens*): Product yield prediction and biochar formation mechanism. Bioresour. Technol. 263, 444–449. https://doi.org/10.1016/j.biortech.2018.05.040.

Wang, H.-S., Zhao, L.-H., Chen, L.-B., Liang, Y.-F., Tang, J.-Q., 2025b. Study on the adsorption performance of tetracycline by $KMnO_4$/KOH co-modified cow dung-based biochar. Res. Chem. Inter. 51 (4), 2171–2196. https://doi.org/10.1007/s11164-025-05543-2.

Wang, M., Wang, Y., Liu, J., Yu, H., Liu, P., Yang, Y., Sun, D., Kang, H., Wang, Y., Tang, J., Fu, C., Peng, L., 2024a. Integration of advanced biotechnology for green carbon. Green. Carbon 2 (2), 164–175. https://doi.org/10.1016/j.greenca.2024.02.006.

Wang, Y., Fan, C., Hu, H., Li, Y., Sun, D., Wang, Y., Peng, L., 2016. Genetic modification of plant cell walls to enhance biomass yield and biofuel production in bioenergy crops. Biotechnol. Adv. 34 (5), 997–1017. https://doi.org/10.1016/j.biotechadv.2016.06.001.

Wang, Y., Wen, J., Li, S., Li, J., Yu, H., Li, Y., Ren, X., Wang, L., Tang, J., Zhang, X., Liu, Z., Peng, L., 2024b. Upgrading pectin methylation for consistently enhanced biomass enzymatic saccharification and cadmium phytoremediation in rice *Ospmes* site-mutants. Int J. Biol. Macromol. 262, 130137. https://doi.org/10.1016/j.ijbiomac.2024.130137.

Wang, Y., Zhang, H., Li, Y., Yu, H., Sun, D., Yang, Y., Zhang, R., Yu, L., Ma, F., Aftab, M. N., Peng, L., Wang, Y., 2025c. Effective xylan integration for remodeling biochar uniformity and porosity to enhance chemical elimination and CO_2 adsorption. Int J. Biol. Macromol. 291, 138865. https://doi.org/10.1016/j.ijbiomac.2024.138865.

Wang, H., Li, S., Wu, L., Zou, W., Zhang, M., 2025d. Semi-overexpressed OsMYB86L2 specifically enhances cellulose biosynthesis to maximize bioethanol productivity by cascading lignocellulose depolymerization via integrated rapid-physical and recyclable-chemical processes. Green. Chem. 27, 9127–9143. https://doi.org/10.1039/D5GC00658A.

Xiang, Y., Cheng, C.-Y., Lu, K.-F., Bai, W.-C., Zang, Z.-X., Xu, L., Liu, G.-J., 2025. Ligand removal and metal exchange tailoring of HP-MOFs for gold recovery from electronic waste. Sep Purif. Technol. 365, 132647. https://doi.org/10.1016/j.seppur.2025.132647.

Xie, J., Lin, R., Liang, Z., Zhao, Z., Yang, C., Cui, F., 2021. Effect of cations on the enhanced adsorption of cationic dye in Fe_3O_4-loaded biochar and mechanism. J. Environ. Chem. Eng. 9 (4), 105744. https://doi.org/10.1016/j.jece.2021.105744.

Yang, H., Yu, Y., Zhang, H., Wang, W., Zhu, J., Chen, Y., Zhang, S., Chen, H., 2024. Effect mechanism of phosphorous-containing additives on carbon structure evolution and biochar stability enhancement. Biochar 6 (1), 39. https://doi.org/10.1007/s42773-024-00330-5.

Yu, H., Hu, M., Hu, Z., Liu, F., Yu, H., Yang, Q., Gao, H., Xu, C., Wang, M., Zhang, G., Wang, Y., Xia, T., Peng, L., Wang, Y., 2022. Insights into pectin dominated enhancements for elimination of toxic Cd and dye coupled with ethanol production in desirable lignocelluloses. Carbohydr. Polym. 286, 119298. https://doi.org/10.1016/j.carbpol.2022.119298.

Yu, H., Zhang, G., Liu, J., Liu, P., Peng, H., Teng, Z., Li, Y., Ren, X., Fu, C., Tang, J., Li, M., Wang, Y., Wang, L., Peng, L., 2025. A functional cascading of lignin modification via repression of caffeic acid *O*-methyltransferase for bioproduction and anti-oxidation in rice. J. Adv. Res. https://doi.org/10.1016/j.jare.2025.01.048.

Zhang, D., He, Q., Hu, X., Zhang, K., Chen, C., Xue, Y., 2021a. Enhanced adsorption for the removal of tetracycline hydrochloride (TC) using ball-milled biochar derived from crayfish shell. Colloid Surf. A 615, 126254. https://doi.org/10.1016/j.colsurfa.2021.126254.

Zhang, G., Wang, L., Li, X., Bai, S., Xue, Y., Li, Z., Tang, S.-w, Wang, Y., Wang, Y., Hu, Z., Li, P., Peng, L., 2021b. Distinctively altered lignin biosynthesis by site-modification of *OsCAD2* for enhanced biomass saccharification in rice. Gcb Bioenergy 13 (2), 305–319. https://doi.org/10.1111/gcbb.12772.

Zhang, R., Gao, H., Wang, Y., He, B., Lu, J., Zhu, W., Peng, L., Wang, Y., 2023a. Challenges and perspectives of green-like lignocellulose pretreatments selectable for low-cost biofuels and high-value bioproduction. Bioresour. Technol. 369, 128315. https://doi.org/10.1016/j.biortech.2022.128315.

Zhang, W., Du, C., Zhang, N., Zheng, Z., Tie, J., 2022. Reactive blue 19 adsorption behaviors of magnesium hydroxide modified biochar derived from the traditional Chinese medical residual. J. Indian Chem. Soc. 99 (7), 100517. https://doi.org/10.1016/j.jics.2022.100517.

Zhang, Y., Zhang, J., Chen, K., Shen, S., Hu, H., Chang, M., Chen, D., Wu, Y., Yuan, H., Wang, Y., 2023b. Engineering banana-peel-derived biochar for the rapid adsorption of tetracycline based on double chemical activation. Resour. Conserv. Recycl. 190, 106821. https://doi.org/10.1016/j.resconrec.2022.106821.

Zhao, C., Ma, J., Li, Z., Xia, H., Liu, H., Yang, Y., 2020. Highly enhanced adsorption performance of tetracycline antibiotics on KOH-activated biochar derived from reed plants. RSC Adv. 10 (9), 5066–5076. https://doi.org/10.3390/toxics12100691.

Zhao, X., Liu, M., Feng, H., Luo, X., Yang, Y., Hu, J., Hu, Y., 2024. Effects and mechanisms on Cr(VI) and methylene blue adsorption by acid $(NH_4)_2S_2O_8$ modified sludge biochar. Sep Purif. Technol. 345, 127100. https://doi.org/10.1016/j.seppur.2024.127100.

Zhou, J., He, Y., Huang, L., Xu, A., Zhao, Y., Wang, J., He, G., Fan, S., Huang, Z., 2024. Preparation of magnetic biochar from macadamia nutshell pretreated by $FeCl_3$-assisted mechanochemical activation for adsorption of heavy metals. J. Environ. Chem. Eng. 12 (4), 113122. https://doi.org/10.1016/j.jece.2024.113122.